Influence of atmospheric and sea-surface corrections on retrieval of bottom depth and reflectance using a semi-analytical model: a case study in Kaneohe Bay, Hawaii

James A. Goodman,[1,*] ZhongPing Lee,[2] and Susan L. Ustin[3]

[1]Bemard M. Gordon Center for Subsurface Sensing and Imaging Systems, University of Puerto Rico at Mayagüez, P.O. Box 9048, Mayagüez, Puerto Rico 00681, USA

[2]U.S. Naval Research Laboratory, Code 7333, Stennis Space Center, Mississippi 39529, USA

[3]Department of Land, Air and Water Resources, Center for Spatial Technologies and Remote Sensing, University of California, Davis, One Shields Avenue, Davis, California 95616, USA

*Corresponding author: jgoodman@uprm.edu

Received 18 March 2008; accepted 23 April 2008;
posted 29 May 2008 (Doc. ID 93866); published 11 June 2008

Hyperspectral instruments provide the spectral detail necessary for extracting multiple layers of information from inherently complex coastal environments. We evaluate the performance of a semi-analytical optimization model for deriving bathymetry, benthic reflectance, and water optical properties using hyperspectral AVIRIS imagery of Kaneohe Bay, Hawaii. We examine the relative impacts on model performance using two different atmospheric correction algorithms and two different methods for reducing the effects of sunglint. We also examine the impact of varying view and illumination geometry, changing the default bottom reflectance, and using a kernel processing scheme to normalize water properties over small areas. Results indicate robust model performance for most model formulations, with the most significant impact on model output being generated by differences in the atmospheric and deglint algorithms used for preprocessing. © 2008 Optical Society of America

OCIS codes: 010.0010, 010.0280, 100.3190, 110.2960, 110.4234, 280.0280.

1. Introduction

Remote sensing of shallow aquatic environments provides fundamental information needed for the effective assessment, monitoring, and management of these valuable natural ecosystems. The synoptic capabilities of remote sensing offer the quantitative ability to obtain spatially explicit data over extensive study areas that would otherwise be logistically difficult to obtain. The derived information contributes to analysis of spatially distributed environmental relationships, as well as providing base maps for planning and management. However, there are many challenges and a number of physical limitations related to remote sensing of aquatic environments, mostly as a function of the complex energy interactions in the water and at the air–water interface, the strong absorption and scattering properties of water and its constituents, and the inherent spatial heterogeneity of water optical properties and benthic composition. Nonetheless, advances in instrument capabilities and an increasing sophistication in the available analysis methods, particularly in the field of hyperspectral remote sensing, are addressing these challenges and facilitating greater complexity in the level of scientific questions that can be addressed using remote sensing.

Hyperspectral data have been utilized for deriving information on coastal water properties

0003-6935/08/2800F1-11$15.00/0
© 2008 Optical Society of America

20090306216

and constituents [1–5], extracting information on benthic habitat composition [6–9], and estimating bathymetry [10,11]. In most cases, these independent objectives are achieved using various simplifying assumptions to significantly reduce system complexity (e.g., assuming spatially uniform water properties while deriving information on habitat composition). In contrast, there is an emerging class of algorithms that are being used to simultaneously derive multiple layers of information from a single image [12–20]. These algorithms typically follow physically based approaches. Although empirical relationships and simplifications are still utilized, they maintain spatial variability in the parameters of interest and thereby present a more comprehensive solution to the inverse problem.

One of the algorithms that is being increasingly applied is the semi-analytical inversion model developed by Lee *et al.* [18,19]. This model utilizes a nonlinear optimization scheme to derive estimates of water properties, bathymetry, and bottom reflectance given surface remote sensing reflectance as input without requiring any *a priori* knowledge of environmental parameters. Output from the model includes estimates of P, the phytoplankton absorption coefficient at 440 nm; G, the absorption coefficient for gelbstoff and detritus at 440 nm; BP, a variable representing the combined influences from the particle-backscattering coefficient, view angle, and sea state; B, the bottom albedo at 550 nm; and H, the water depth. Application of this model has focused mostly on its stand-alone implementation [21–23]but has recently also been utilized as the foundation for spectral unmixing analysis of benthic composition [17,24]. In addition to the testing completed during model development, these applications have further confirmed effectiveness of the model across different geographic locations (Tampa Bay, Florida Keys, Bahamas, Hawaii, Puerto Rico) and across different sensor systems (AVIRIS, HYPERION).

As this model increases in use, there is a need to investigate and explain the influence of different model inputs on its performance. We illustrate the impacts of using different atmospheric (ACORN, Tafkaa) and sunglint correction options [19,25], of using different assumptions for view and illumination geometry, and of using different default spectra to represent the normalized bottom reflectance. We also investigate the effectiveness of using a moving kernel in the optimization process to locally average water column properties while retaining independent estimations of bathymetry and bottom reflectance. Model results are evaluated using AVIRIS data from Kaneohe Bay, Hawaii, with lidar bathymetry data and *in situ* benthic reflectance as measured ground truth.

2. Data

A. Study Area

The study area for this project, Kaneohe Bay, is located on the northeast (windward) shore of Oahu, Hawaii (Fig. 1). Kaneohe Bay is a partially enclosed embayment, containing a sizeable lagoon area, extensive fringing reefs, more than 60 individual patch reefs, a protecting barrier reef, natural and man-made channels, colonized and uncolonized hardbottom areas, and extensive regions of unconsolidated sediments (e.g., sand and mud). The shallow fringing reefs are present along most of the shoreline, with natural breaks at stream outlets and artificial breaks where boat channels have been dredged. The patch reefs are located throughout the bay, some having diameters up to 1000 m, and typically extend from the lagoon bottom nearly to the water surface. The barrier reef, which is more than 5 km long and 2 km in width, bounds the ocean side of the bay. The landward side of the barrier reef contains a shallow reef flat transitioning into an extensive sand flat, and the offshore seaward side consists of a steep reef slope. Water clarity varies significantly in the bay, ranging from relatively clear conditions in the open northwest portion of the bay to poor conditions in the partially enclosed southeast portion of the bay. Habitat composition also varies, including typical heterogeneous reef environments as well as regions that are coral or algae dominated. Kaneohe Bay is thus suitably varied to test model performance in a range of natural environmental conditions.

B. Hyperspectral Imagery

AVIRIS hyperspectral imagery was acquired over extensive areas of the Hawaiian Islands in early 2000. All imagery was collected from onboard a NASA ER-2 (a civilian high-altitude reconnaissance platform) from an altitude of 20 km, producing a nominal pixel size of 17 m and a swath width of approximately 10 km. AVIRIS is a "whisk broom" scanner that uses a combination of three detector types to measure 224 contiguous spectral bands (channels) from 370 to 2500 nm at a nominal spectral resolution of 10 nm [26,27]. Raw AVIRIS data are radiometrically

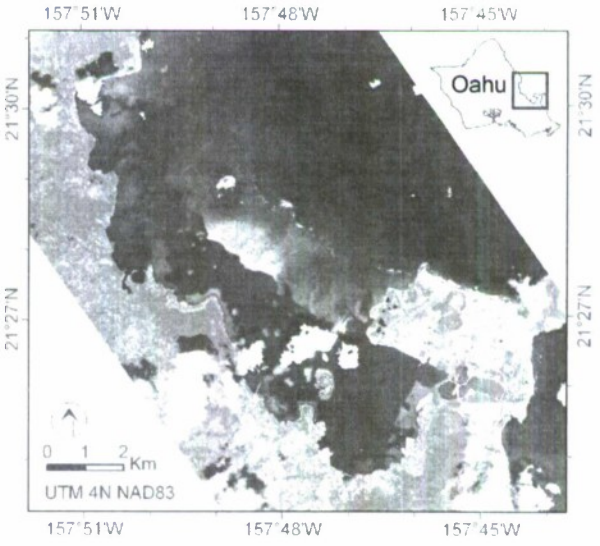

Fig. 1. AVIRIS imagery of Kaneohe Bay, Oahu, Hawaii.

corrected by NASA's Jet Propulsion Laboratory and delivered to the user in units of radiance ($\mu Wcm^{-2}nm^{-1}sr^{-1}$). The imagery for Kaneohe Bay was extracted from a longer flightline covering the entire northeast coast of Oahu acquired at 12:12 pm LST (22:12 GMT) on 12 April, 2000. All image analysis products were georectified using 14 ground control points (RMS = 0.80) with a first degree polynomial and nearest neighbor resampling to produce an output image with 20 m pixels (UTM, Zone 4, NAD83). Before processing, the imagery was also subset to the 42 bands from 400 to 800 nm, and areas of land, clouds, cloud shadow, and deep water (>40 m) were masked to improve computational efficiency.

C. Lidar Bathymetry

Bathymetry data for Kaneohe Bay was acquired by the U.S. Army Corps of Engineers Joint Airborne Lidar Bathymetry Technical Center of Expertise (JALBTCX) using the Scanning Hydrographic Operational Airborne Lidar Survey (SHOALS). SHOALS is an airborne instrument that uses short pulses of light at two different wavelengths (532 and 1064 nm) to derive estimates of water depth [28,29]. The vertical accuracy of the system is ±15 cm, and the horizontal accuracy is ±3 m using differential GPS (±1 m when using kinematic GPS from local stations) [28]. Under ideal conditions the maximum resolvable depth of the SHOALS system approaches 60 m, but actual water conditions are typically more limiting and dictate a shallower practical limit.

The SHOALS measurements for Kaneohe Bay were performed in early 2000 and thus nearly contemporaneous with the AVIRIS data collection. The delivered data format was a series of irregularly spaced *xyz* points with a positional accuracy of ±3 m and a sampling density of 0.06 pulses/m^2, which equates to one pulse (or one depth measurement) for every 16 m^2 (i.e., 4 m pixel). The bathymetric data thus needed to be spatially interpolated and resampled to the same geographic projection and spatial resolution as the AVIRIS imagery (UTM, Zone 4, NAD83, 20 m pixels). The interpolation process was performed using a spline function to first create a grid of 4 m pixels, and then using spatial averaging to generate 20 m pixels. A correction was also included in the final SHOALS image to reflect tidal conditions at the time of AVIRIS image acquisition (+0.1 m above mean lower low water; NOAA water level station #1612480 in Kaneohe Bay). The resulting SHOALS measurements indicated the appropriate maximum depths of 15–20 m within Kaneohe Bay and extended offshore to an apparent detection limit of ~30 m outside the bay.

D. Field Spectra

Measurements of *in situ* underwater bidirectional reflectance were collected for sand, coral and algae in Kaneohe Bay during October 2001 and April 2002. A statistical analysis revealed no significant difference between average spectra from the different dates, and because there were no major intervening environmental disturbances, the data were assumed representative of reflectance characteristics in 2000. Measurements were performed using a modified GER-1500 spectrometer (Spectra Vista Corp., Poughkeepsie, N.Y.) encased within a custom underwater housing. The GER-1500 is a field-portable instrument that measures 512 spectral bands in the region from 350 to 1050 nm at a resolution of 1.5 nm. The instrument was configured with an 8° full-angle foreoptic, used automatic integration speed, and averaged four detector scans for every saved spectrum. Measurements were acquired *in situ* using a shadowing protocol to minimize effects from fluctuating underwater light conditions [30,31]. A 99% Spectralon panel (Labsphere, Inc., North Sutton, N.H.) was used for reference measurements, and reflectance was calculated as the ratio of each target spectrum to its associated reference spectrum.

The field spectra served two different purposes in the analysis, as ground truth for evaluating model estimates of benthic reflectance and as different model inputs for the default normalized bottom reflectance. For use as ground truth, sand spectra were measured from a total of 12 distinct areas (locations recorded with GPS), each approximately 10,000 m^2 in extent, relatively level, spatially homogeneous, and distributed at different locations and depths throughout the study area. Data were collected from 40 to 60 random locations in each sand area, and subsequently used to generate a set of 12 average spectra. For use as the normalized bottom reflectance, all sand measurements were grouped to create a single average sand spectrum, and numerous additional measurements ($n = 254$ from dominant coral species *P. compressa* and *M. capitata*; $n = 174$ from dominant algae species *D. cavernosa* and *G salicornia*) were used to produce average coral and algae spectra. The final sand, coral, and algae spectra were normalized to 1 at 550 nm and spectrally resampled to match AVIRIS for use as input to the model (Fig. 2).

3. Methods

A. Atmospheric Correction and Deglint

Atmospheric correction algorithms calibrate imagery from at-sensor radiance to reflectance at the water surface, and deglint algorithms are utilized to remove, or minimize, the effects of specular reflection at the water surface (i.e., sunglint). Because these two preprocessing corrections are interrelated, a complete solution to the problem is to integrate the two procedures and resolve both the atmospheric and glint corrections simultaneously (as suggested by [32,33]). In the absence of any readily available integrated algorithms, however, it is common to instead independently apply the two correction algorithms. We follow this independent approach and examine the resulting impact on performance of the inversion model using two different atmospheric

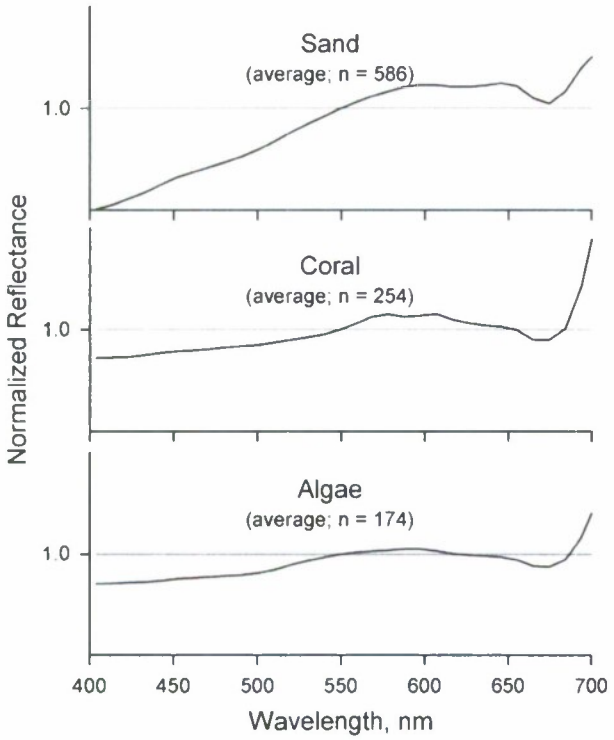

Fig. 2. Normalized average field spectra, shown with spectral resampling to match AVIRIS spectral characteristics.

correction algorithms, ACORN (v. 4.0) and Tafkaa (v. 2003), and two different deglint algorithms [19,25]. The deglint algorithms selected for this study are representative of two different correction schemes: one algorithm uses an independent correction for every pixel [19], and the other algorithm uses a subset of the image to determine correction parameters for the entire image [25].

ACORN (Analytical Imaging and Geophysics, LLC, Boulder, Colo.) utilizes at-sensor radiance data as input and employs MODTRAN-based radiative transfer calculations to produce estimates of apparent surface reflectance [34]. The algorithm was run in Mode 1 (hyperspectral atmospheric correction of complete image) with a tropical atmospheric model, using the 940 and 1140 nm bands to derive water vapor and allowing the model to estimate atmospheric visibility. ACORN provides three options to account for residual artifacts in the reflectance output: type 1 corrects for spectral mismatch between instrument calibration and the radiative transfer algorithm occurring at strong atmospheric absorption features (760, 940, 1150, and 2000 nm), type 2 suppresses minor artifacts throughout the spectrum associated with errors in the radiometric calibration and radiative transfer equations, and type 3 adjusts the portions of the spectrum around the 1400 and 1900 nm water vapor bands with low measured radiance to zero [34]. To investigate differences in output, ACORN was run using two options, one with all artifact suppression options (types 1, 2, and 3) and one with no artifact suppression options. Additionally, to match the input requirements of the semi-analytical optimization model, ACORN output, R_{ACORN}, was converted to remote sensing reflectance, R_{rs} (defined as the ratio of water leaving radiance to the downwelling irradiance on the surface) according to $R_{\mathrm{rs}} = R_{\mathrm{ACORN}}/\pi$.

Tafkaa (U.S. Naval Research Laboratory, Washington, DC) is a hyperspectral atmospheric correction algorithm developed specifically to address the confounding variables associated with shallow water applications [35–37]. The algorithm is an extensively modified version of ATREM [38,39] that employs a lookup table approach to estimate remote sensing reflectance based on the spectral characteristics of the at-sensor radiance data. The algorithm was run using a tropical atmospheric model, including an array of gaseous absorption calculations (H_2O, CO_2, O_3, N_2O, CO, CH_4, O_2), excluding urban aerosols, and assigning the 1040, 1240, 1640, and 2250 nm bands as wavelengths with no apparent water leaving radiance. Corrections using these parameters were performed using two separate analysis options. The first option used a rectangular deep-water subset for determining the aerosol type and optical depth and used nadir viewing geometry for calculating atmospheric absorption and scattering. The second option followed similar computations but was operated on a pixel-by-pixel basis to explicitly account for varying view and illumination geometry throughout the scene.

The first deglint option used a 750 nm normalizing scheme derived from Lee *et al.* [19], which assumes that reflectance at 750 nm should approach zero but that situations exist where this reflectance is greater than zero (e.g., shallow areas in clear water). The sunglint correction is calculated as a constant offset across all wavelengths such that reflectance at 750 nm is equal to a spectral constant, Δ. For raw remote sensing reflectance, $R_{\mathrm{rs}}{}^{\mathrm{raw}}(\mathrm{sr}^{-1})$, as derived through atmospheric correction, an approximation of surface remote sensing reflectance, $R_{\mathrm{rs}}(\mathrm{sr}^{-1})$, is determined by

$$R_{\mathrm{rs}}(\lambda) = R_{\mathrm{rs}}{}^{\mathrm{raw}}(\lambda) - R_{\mathrm{rs}}{}^{\mathrm{raw}}(750) + \Delta, \quad (1)$$

$$\Delta = 0.000019 + 0.1\,[R_{\mathrm{rs}}{}^{\mathrm{raw}}(640) - R_{\mathrm{rs}}{}^{\mathrm{raw}}(750)]. \quad (2)$$

The second deglint option follows Hochberg *et al.* [25], which also assumes water leaving radiance in the near-infrared (NIR) should approach zero. The relative intensity of sunglint, f_g, and the absolute sunglint intensity, $R_{\mathrm{rs}}{}^{\mathrm{glint}}(\lambda)$, are both derived using minimum and maximum data from a spatial subset of uniform deep water. In this case, the subset was selected to extend across a deep-water section encompassing the full characteristics of the cross-track sunglint. Glint correction for the image is calculated as

$$R_{\mathrm{rs}}(\lambda) = R_{\mathrm{rs}}{}^{\mathrm{raw}}(\lambda) - f_g R_{\mathrm{rs}}{}^{\mathrm{glint}}(\lambda). \quad (3)$$

B. Semi-Analytical Inversion Model

The semi-analytical model described by Lee *et al.* [18,19] presents an inversion scheme for retrieving estimates of water optical properties, bathymetry, and albedo at 550 nm from measured values of remote sensing reflectance at the water surface. An overview is presented below. The model first defines a relationship between R_{rs} and subsurface r_{rs} (sr^{-1}), the ratio of upwelling radiance to downwelling radiance evaluated just below the air–water interface:

$$R_{rs} = \frac{0.5 r_{rs}}{1 - 1.5 r_{rs}}, \tag{4}$$

where the numerator accounts for transmission through the air–water interface and the denominator accounts for the effects of internal reflectance (note that the explicit dependence on wavelength has been dropped for convenience). The governing equation of the semi-analytical inversion model is then defined by

$$r_{rs} \approx \underbrace{r_{rs}^{dp}\left(1 - \exp\left\{-\left[\frac{1}{\cos(\theta_w)} + \frac{D_u^{C}}{\cos(\theta)}\right]\kappa H\right\}\right)}_{\text{Water column contribution}} + \underbrace{\frac{1}{\pi}\rho_b B \times \exp\left\{-\left[\frac{1}{\cos(\theta_w)} + \frac{D_u^{B}}{\cos(\theta)}\right]\kappa H\right\}}_{\text{Bottom contribution}}, \tag{5}$$

where $r_{rs}^{dp}(sr^{-1})$ is the subsurface remote sensing reflectance for optically deep water; θ_w(rad) is the subsurface solar zenith angle; θ(rad) is the subsurface view angle; $\kappa(m^{-1})$ is the summation of the total backscattering and absorption coefficients; H(m) is water depth; D_u^{C} and D_u^{B} are the optical path elongation factors for scattered photons from the water column and bottom, respectively; ρ_b is a representative bottom spectrum normalized to 1 at 550 nm; and B is the bottom albedo (reflectance) at 550 nm. The components r_{rs}^{dp}, κ, D_u^{C}, and D_u^{B} are further defined as functions of the absorption coefficient for gelbstoff and detritus at 440 nm, G (m^{-1}), the phytoplankton absorption coefficient at 440 nm, P (m^{-1}), and a combined variable representing the influences from the particle-backscattering coefficient, view angle, and sea state, BP (m^{-1}). Ultimately, hyperspectral R_{rs} becomes approximated as a function of just five unknown variables:

$$R_{rs} = f\{P, G, BP, B, H\}. \tag{6}$$

The model is solved using constrained nonlinear optimization to produce estimates of remote sensing reflectance, R_{rs}^{est}, by iteratively adjusting values for P, G, BP, B, and H such that the difference between R_{rs} and R_{rs}^{est} is minimized. The model requires no *a priori* information on environmental characteristics. We have implemented this model in the Interactive Data Language (Research Systems, Inc., Boulder, Colo.) as part of an aquatic analysis package called AquaCor. Under this framework, model optimization is achieved utilizing a generalized reduced-gradient algorithm to solve the following objective function:

$$\min \frac{\|R_{rs}(\lambda) - R_{rs}^{est}(\lambda, P, G, BP, B, H)\|_2}{\|R_{rs}(\lambda)\|_2}$$

$$\text{for } \lambda \in \begin{pmatrix} 400 \rightarrow 675 \\ 720 \rightarrow 800 \end{pmatrix} \text{subject to} \begin{cases} 0.005 \le P \le 0.5 \\ 0.002 \le G \le 3.5 \\ 0.001 \le BP \le 0.5 \\ 0.01 \le B \le 0.6 \\ 0.2 \le H \le 33.0 \end{cases}, \tag{7}$$

where $\|x\|_2$ is the Euclidean norm defined by $\sqrt{\sum (x_n)^2}$.

C. Kernel Processing

The overall model operates separately on every pixel in the image, with no information shared between any of the adjacent pixels. Although this pixel-independent approach is appropriate for bathymetry and bottom albedo estimations in most situations, particularly in heterogeneous reef environments, it can be argued that water properties are not likely to vary significantly at the pixel scale and a different approach is required for these parameters. Following this logic, we introduce a new processing capability for the inversion model that maintains independence of the bathymetry and albedo parameters but imposes spatial uniformity in water properties within a moving kernel of pixels (i.e., 3×3, 5×5, etc.). This is achieved by expanding the objective function used for solving each pixel to incorporate its surrounding pixels:

$$\min \sum_{i,j=1}^{n} \frac{\|R_{rs\,ij}(\lambda) - R_{rsij}^{est}(\lambda, P, G, BP, B_{ij}, H_{ij})\|_2}{\|R_{rs\,ij}(\lambda)\|_2},$$

for n = odd numbers ≥ 3 and subject to the same parameter constraints and range of wavelengths as in Eq. (7). This approach still obtains an independent solution for every pixel but allows localized uniformity in water properties.

D. Analysis Procedure

Analysis is performed by implementing the inversion model using a series of different preprocessing schemes and model formulations:

- A qualitative analysis is first used to evaluate output from the different combinations of atmospheric and deglint algorithms.
- The SHOALS data are used as ground truth to evaluate differences in model estimated bathymetry resulting from the different preprocessing algorithms.
- The SHOALS data are used as ground truth to examine differences in two different scenarios for subsurface view and illumination angles: (1) using

a constant nadir for both view and illumination angles ($\theta = \theta_w = 0°$) and (2) using the AVIRIS navigation files to generate pixel-specific view and illumination angles.

– Bathymetry estimates are next evaluated for four different spectra representing the default bottom reflectance: sand, coral, algae, and a flat spectrum with all wavelengths set to 1.0.

– Bathymetry estimates are then evaluated for two different options of the kernel processing scheme, using 3×3 and 5×5 kernels.

– A final evaluation examines model estimated reflectance at 550 nm (parameter B) compared with the *in situ* reflectance spectra measured at the 12 sand locations.

4. Results and Discussion

A. Preprocessing Algorithms

The AVIRIS imagery used in this study was collected for terrestrial applications on Oahu, and because it was not optimized for aquatic analysis, the resulting view and illumination geometry produced significant cross-track sunglint in the water portions of the image. This provides the opportunity to evaluate the combined effectiveness of the atmospheric and sunglint removal algorithms in less than ideal conditions, under which the capacity for properly correcting the image becomes significantly more important.

The first step in this evaluation is to examine the output from the four different atmospheric correction options. Figure 3 illustrates average cross-track reflectance at 750 nm over deep water and a spectral profile of reflectance over a shallow submerged sand area as produced by these different options. Surface reflectance in the NIR over deep water should approach zero, however, as shown in Fig. 3(a) most of the atmospheric correction routines do not properly achieve this result. Both of the ACORN options and the Tafkaa option using the deep water subset retain significant influence from the cross-track sunglint. In contrast, although the Tafkaa option using full geometry produces minor negative reflectance values, its correction does effectively remove the cross-track effect. For the shallow sand area (Fig. 3(b)) the full geometry Tafkaa option again produces acceptable results, while the three other options produce a profile with similar spectral shape but with an inappropriate upward shift in the overall magnitude of reflectance. The ACORN option with artifact suppression also exhibits an anomalous overcorrection in the wavelengths closest to 400 nm (depicted as increased reflectance in shorter wavelengths), which is attributed to the artifact suppression algorithms. As with the cross-track analysis, the upward shift in the spectra is considered a function of uncorrected sunglint effects. It is concluded that the full geometry Tafkaa option produces the best initial results but that atmospheric correction alone is not sufficient to fully correct for the sunglint effects.

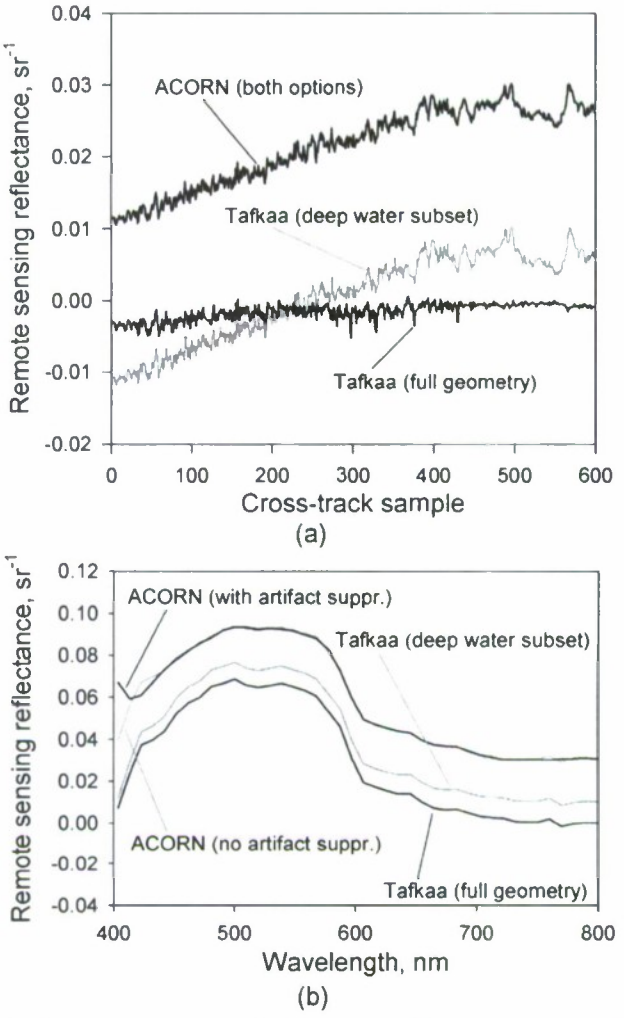

Fig. 3. Remote sensing reflectance output following atmospheric correction: (a) 10-line cross-track average of deep water at 750 nm, (b) 9-pixel average spectral profile for submerged sand at 3 m depth.

The two deglint algorithms were subsequently applied to the atmospherically corrected data to remove the cross-track and wave-induced sunglint. Results are illustrated in Figs. 4 and 5 using the same deep water region and shallow sand area as used in Fig. 3. It is immediately apparent from this comparison that the 750 nm normalizing scheme (Fig. 5) consistently generates the best results. This scheme removes the cross-track sunglint effects, produces reflectance values near zero in deep water at 750 nm, and results in closely similar spectral profiles for the shallow sand area. In contrast, the Hochberg *et al.* deglint algorithm (Fig. 4) still retains some of the cross-track effects, which are evident as positive (undercorrected) and negative (overcorrected) offsets in the spectral output. These offsets result because a single correction relationship is applied across the entire scene, whereas the cross-track effects introduce the need for a variable relationship. Although the Hochberg *et al.* algorithm, and other similar approaches (e.g., [40]), have proved effective at

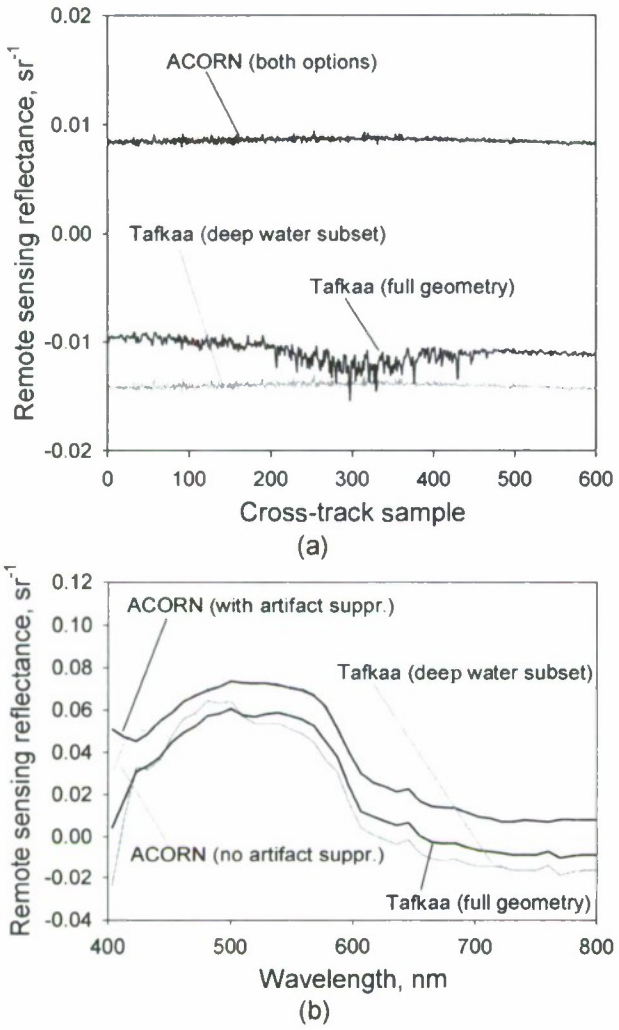

Fig. 4. Remote sensing reflectance output following atmospheric correction and Hochberg *et al.* deglint algorithm: (a) 10-line cross-track average of deep water at 750 nm, (b) 9-pixel average spectral profile for submerged sand at 3 m depth.

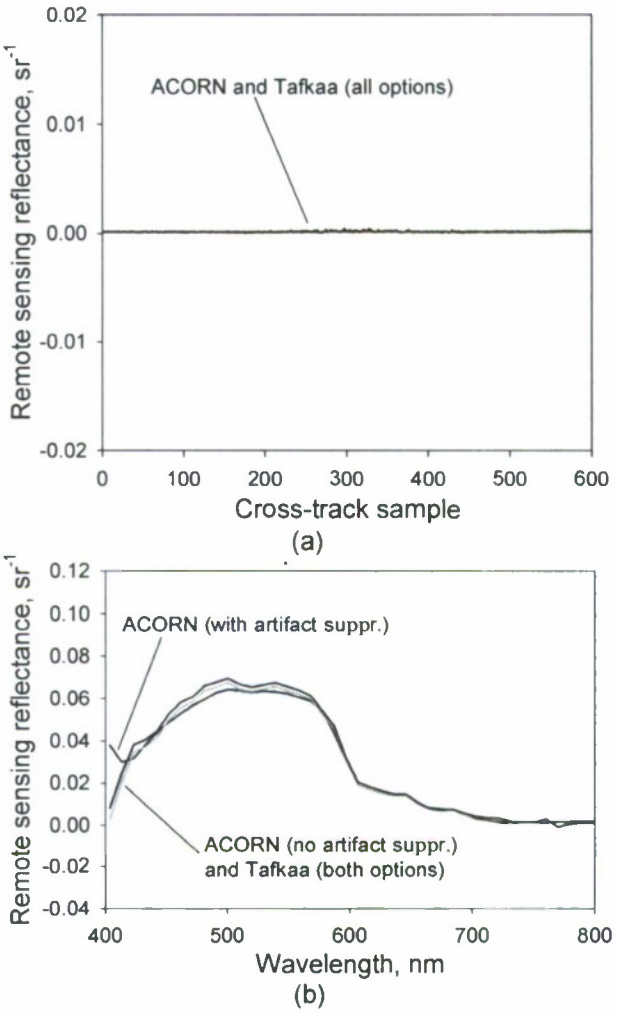

Fig. 5. Remote sensing reflectance output following atmospheric correction and 750 normalizing deglint algorithm: (a) 10-line cross-track average of deep water at 750 nm, (b) 9-pixel average spectral profile for submerged sand at 3 m depth.

removing wave-induced sunglint, cross-track corrections require a more dynamic approach. As illustrated here, the 750 nm normalizing method, where corrections are independently performed on each pixel, represents a viable solution to this issue.

We next implemented the inversion model using 12 different preprocessing scenarios and performed a quantitative analysis of model estimated bathymetry for each scenario using the SHOALS bathymetry data as ground truth. Results from this analysis are presented in Table 1, specifying the regression coefficient, r, the slope of linear least-squares fit, m, and the average absolute difference, a, for each scenario from 0 to 20 m water depth. The best overall scenario was the combination of full geometry Tafkaa with the 750 nm normalizing algorithm for deglinting. This scenario exhibited a strong, nearly one-to-one, correlation ($r = 0.9$, $m = 1.03$), with an average absolute difference of 1.6 m for depths from 1 to 20 m (Fig. 6), which indicates a robust capacity for estimating bathymetry. The strength of this relationship is also particularly encouraging considering there are some acknowledged residual errors resulting from misregistration and spatial resampling. The best performance is achieved in depths from 0 to 7 m, with overestimation observed in depths greater than 7 m. Other applications of the inversion model have shown strong bathymetric agreement for depths of 15 m or greater [19,23]. Hence, we attribute the overestimation in this case to be a function of the water optical properties in Kaneohe Bay, where water clarity is relatively limited compared with typical reef environments.

Other promising results included the Tafkaa option using the deep water subset and the ACORN option with no artifact suppression, both combined with the 750 nm normalizing algorithm, as well as the full geometry Tafkaa option with no deglint (but all exhibiting either slightly lower regression coefficients or significantly lower slope than the best overall option). All other ACORN options and all of

Table 1. SHOALS Data Versus Estimated Bathymetry (Correlation Coefficient, r; Slope of Best Fit Curve, m; absolute error, a) for 0–20 m Water Depth Using Different Preprocessing Algorithms for Atmospheric Correction and Deglint[a]

	r	m	a
NO Deglint			
ACORN (no artifact suppression)	−0.104	−0.00	6.29 m
ACORN (artifact suppression)	−0.131	−0.00	6.29 m
Tafkaa (deep water subset)	0.682	0.80	3.20 m
Tafkaa (full geometry)	0.894	1.03	1.70 m
Hochberg *et al.* Deglint			
ACORN (no artifact suppr.)	−0.234	−0.01	6.17 m
ACORN (artifact suppr.)	−0.253	−0.01	6.19 m
Tafkaa (deep water subset)	0.486	0.81	4.58 m
Tafkaa (full geometry)	0.780	1.27	3.74 m
750 Normalizing Deglint			
ACORN (no artifact suppr.)	0.912	0.80	1.26 m
ACORN (artifact suppr.)	0.795	0.74	1.76 m
Tafkaa (deep water subset)	0.907	1.13	2.00 m
Tafkaa (full geometry)	0.902	1.03	1.64 m

[a] All model runs were performed using full geometry for view and illumination angles and an average sand spectrum as the default benthic input.

the options with Hochberg *et al.* deglinting did not perform as strongly. It becomes apparent from this analysis that the preprocessing procedure can have a large impact on model output, particularly situations with a large amount of cross-track sunglint. The algorithms selected for further evaluation of the performance of the inversion model were the full geometry Tafkaa option combined with the 750 nm normalizing deglint algorithm.

B. View and Illumination Geometry

Two different scenarios were utilized to investigate the impacts of using different assumptions regarding the view and illumination geometry. One option assumed constant nadir view and illumination angles ($\theta = \theta_w = 0°$), and the other option used information derived from the AVIRIS navigation files to generate pixel-specific angles. Results from this comparison are presented in Table 2. This analysis exhibits negligible differences between the two different view and illumination scenarios. As a caveat, however, the average subsurface solar angle for this scene was only 9.4°, and the analysis area included only the middle third of the AVIRIS image where view angles are lowest (<10°). We hypothesize that these differences will be more substantial for higher view and sun angles and suggest including pixel specific view and illumination information when available.

C. Default Bottom Spectrum

The model includes a default spectrum [ρ_b, in Eq. (5)] that combines with parameter B to serve as a proxy for bottom reflectance $\rho \approx \rho_b B/\pi$. Lee *et al.* [18] originally used a simple spectral constant to represent the default spectrum, and other applications have since used measured sand or seagrass spectra with similar success [17,19,21–23]. Further, Goodman and Ustin [17] found that model performance was not significantly impacted when using different default spectra as input. In order to provide a quantitative indication of this parameter's influence, four different spectra were used as input, three derived from measured field spectra for sand, coral, and algae (Fig. 2) and one spectrum set to a constant

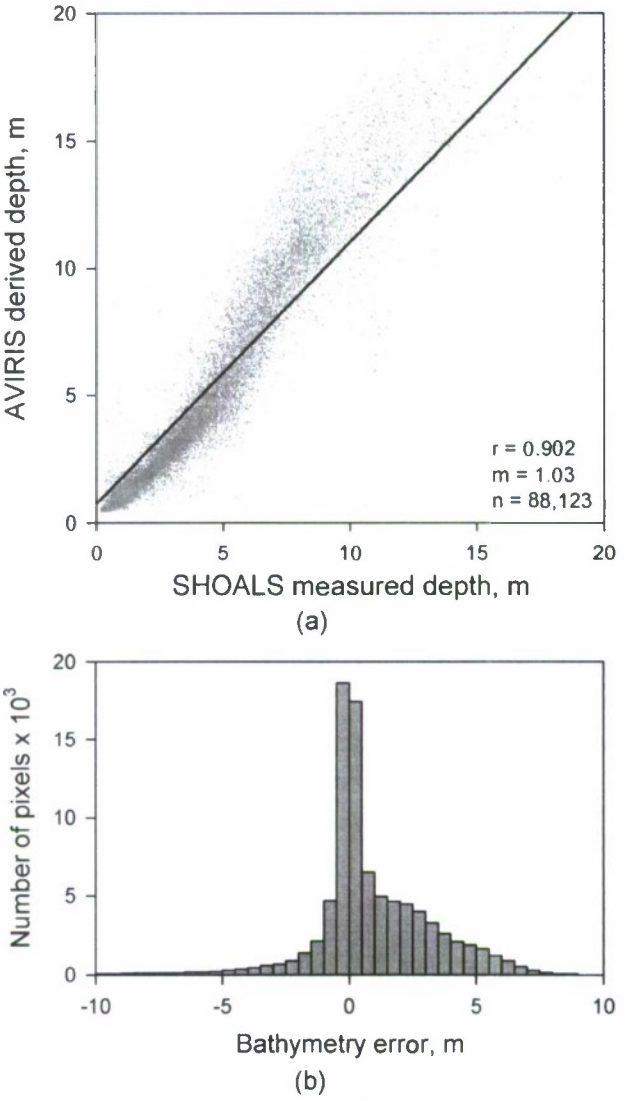

Fig. 6. Bathymetry analysis using full geometry Tafkaa, 750 nm normalizing deglint, full geometry for view and illumination angles, and an average sand spectrum as the default benthic input: (a) scatterplot of model derived bathymetry versus SHOALS bathymetry, (b) histogram of bathymetry errors.

Table 2. SHOALS Data Versus Estimated Bathymetry (Correlation Coefficient, r; Slope of Best Fit Curve, m; Absolute Error, a) for 0–20 m Water Depth Using Different Subsurface View and Illumination Geometries[a]

	r	m	a
Nadir	0.902	1.04	1.66 m
Full Geometry	0.902	1.03	1.64 m

[a] Both model runs were performed using full geometry Tafkaa, 750 nm normalizing deglint, and an average sand spectrum as the default benthic input.

value of 1.0. Results were again analyzed by comparing estimated bathymetry with the measured SHOALS data (Table 3). This comparison indicates only minor variations in the output, despite the differences in the input spectra. Even the flat spectrum produced reasonable output. This favorable functionality is attributed to the fact that optimization is a function of the entire spectrum from 400 to 800 nm, a region where the most significant influence is attenuation in the water column, particularly at longer wavelengths. Thus, the more minor differences in spectral shape associated with the different input spectra are substantially less influential on the optimization. This suggests that within reason the model is not overly sensitive to the input spectrum and that it can be applied over diverse bottom features with minimal impact on performance.

D. Kernel Processing

A final bathymetry analysis was performed using three different kernel processing options: the default 1×1 scenario, as well as 3×3 and 5×5 kernel scenarios. Results are presented in Table 4, where it is evident that the kernel processing option leads to decreasing accuracy for estimating bathymetry. A comparison of other model output parameters confirms that the processing scheme produces greater local uniformity in the water properties, as intended, but at the expense of introducing errors primarily in the bathymetry. Such results are not entirely unexpected, however, particularly in a model limited to only five output parameters, where changes imparted on three of the parameters (P, G, BP) are manifest in changes to the two other parameters (B, H). Further, the computational penalty for including the kernel options increased processing time from 30 min (desktop PC with 3.20 GHz CPU and 1.0 GB RAM) to 24 h for the 3×3 kernel and over 6 days for the 5×5 kernel. Together, these results indicate that the model should retain its original processing architecture of processing each pixel independently.

E. Benthic Reflectance

Another measure of accuracy was evaluated by comparing model-derived estimates of bottom reflectance at 550 nm with measured data at 12 sand areas in Kaneohe Bay. The 12 areas were located at depths varying from 0.5 to 15.5 m and spatially distributed throughout the bay. Average, minimum, and maximum reflectance values at 550 nm were extracted from the merged 2001 and 2002 field data, which were assumed to be representative of reflectance at these same areas in 2000. Additionally, because each of the selected sand areas was reasonably homogeneous, it was also assumed that the average characteristics extracted from the 40–60 point samples at each field location were equivalent to average model estimates at the scale of image pixels. Values for model estimated reflectance at 550 nm (B) were extracted from the image areas corresponding to each of the field sampling locations. Figure 7 illustrates results of the reflectance estimate differences at 550 nm from all 12 sand areas. Reflectance estimates for each area are within the range of measured field data for the majority of the sand areas, and the relative levels of reflectance also generally parallel the trends of lighter and darker sand areas (but with an average positive offset of 9.6%). This offset is partially attributed to scaling errors associated with comparing field measurements with image data but is also suggestive of the need to incorporate a fixed parameter resembling Q for optically shallow waters [41] ($Q = E_u/L_u$, the ratio of upwelling irradiance to upwelling radiance at nadir) in the equation for bottom reflectance (e.g., $\rho \approx \rho_b B/Q$, with $Q < \pi$), rather than the current formulation using π to convert between the radiance and irradiance fields. In this example, $Q = 2.6$ would significantly improve the comparison of estimated reflectance with measured sand reflectance for the 12 sand areas (reducing the average difference to 3%), which is in line with Q values for shallow sand areas measured by Voss *et al.*[41]. This avenue of research warrants further investigation. Nonetheless, because of the general consistency in the reflectance offset, which did not appear to adversely affect the bathymetry estimates, results from the current model formulation were deemed reasonable.

Table 3. SHOALS Data Versus Estimated Bathymetry (Correlation Coefficient, r; Slope of Best Fit Curve, m; Absolute Error, a) for 0–20 m Water Depth Using Different Default Bottom Spectra as Modal Input[a]

	r	m	a
Sand	0.902	1.03	1.64 m
Coral	0.902	0.99	1.48 m
Algae	0.902	1.00	1.50 m
Flat	0.901	0.96	1.40 m

[a]All model runs were performed using full geometry Tafkaa, 750 nm normalizing deglint, and full geometry for view and illumination angles.

Table 4. SHOALS Data Versus Estimated Bathymetry (Correlation Coefficient, r; Slope of Best Fit Curva, m; Absolute Error, a) for 0–20 m Water Depth Using Different Spatial Kernels for Averaging Water Properties[a]

	r	m	a
1×1	0.902	1.03	1.64 m
3×3	0.801	0.85	1.89 m
5×5	0.801	0.81	1.88 m

[a]All model runs performed using full geometry Tafkaa, 750 nm normalizing deglint, full geometry for view and illumination angles, and an average sand spectrum as the default benthic input.

5. Conclusions

Numerous different scenarios were utilized in evaluating output from the semi-analytical model using AVIRIS data from Kaneohe Bay. Model accuracy was primarily assessed using SHOALS bathymetry data but also using measured field reflectance spectra. Results indicated that the most significant influence on

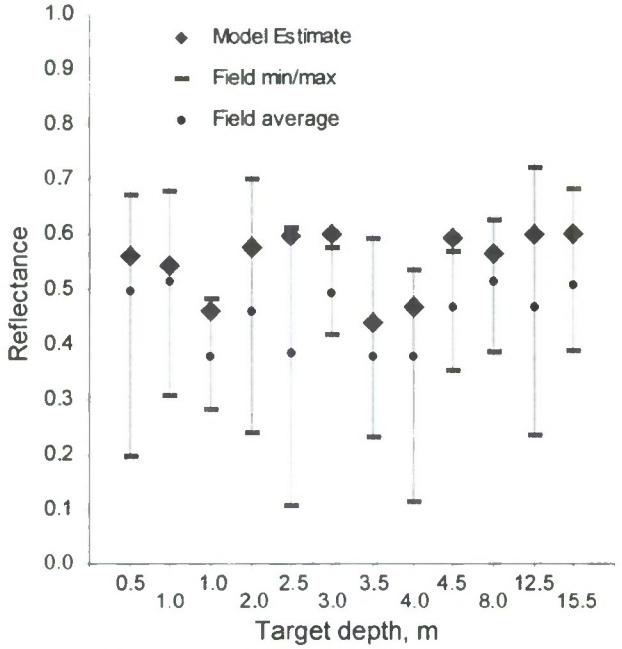

Fig. 7. Comparison of model derived reflectance at 550 nm versus measured data at 12 sand target areas; model derivation performed using full geometry Tafkaa, 750 nm normalizing deglint, full geometry for view and illumination angles, and an average sand spectrum as the default benthic input.

model output was the selection of preprocessing schemes. The best preprocessing option of those considered in this study was the full geometry Tafkaa option for atmospheric correction combined with a straightforward 750 nm normalizing algorithm for deglinting. Results also indicated that incorporating explicit view and illumination geometries within the inversion model has insignificant impact at smaller angles, that the model is not significantly affected by changes in the default bottom spectrum and that a kernel processing scheme for averaging water properties produces decreased accuracy in the bathymetry estimates. By testing and validating the model using AVIRIS imagery from Kaneohe Bay, Hawaii, results from this analysis have demonstrated model transferability and also provided further evidence of its reliability and robust performance capabilities. Furthermore, despite previous limitations on the availability of hyperspectral instruments, which were often limited to research investigations (e.g., AVIRIS, PHILLS), the accessibility and number of commercial airborne instruments continues to increase (e.g., HyMap, CASI, AISA), and even spaceborne data from HYPERION is now available. Therefore, application of the semi-analytical model ultimately extends an important analysis tool to a diversity of other shallow aquatic ecosystems.

This work was supported by NASA Headquarters under Earth System Science Fellowship Grant NGT5-ESS/01-0000-0208. It was also supported by Gordon-CenSSIS, the Bernard M. Gordon Center for Subsurface Sensing and Imaging Systems, under the Engineering Research Centers Program of the National Science Foundation (Award Number EEC-9986821). Additional assistance was provided by the Center for Spatial Technologies and Remote Sensing, the University of California Pacific Rim Research Program, the California Space Institute Graduate Student Fellowship Program, the Canon National Park Science Scholars Program, and NASA's Jet Propulsion Laboratory. Appreciation is also extended to M. Montes and C. Davis at the U.S. Naval Research Laboratory for the Tafkaa model, the U.S. Army Corps of Engineers for the SHOALS bathymetry data, D. Riano for processing of the SHOALS data, the Hawaii Institute of Marine Biology for their support, and P. Sjordal for his untiring assistance in the field.

References

1. V. E. Brando and A. G. Dekker, "Satellite hyperspectral remote sensing for estimating estuarine and coastal water quality," IEEE Transactions on Geoscience and Remote Sensing **41**, 1378–1387 (2003).
2. K. L. Carder, P. Reinersman, R. F. Chen, F. Muller-Karger, C. O. Davis, and M. Hamilton, "AVIRIS calibration and application in coastal oceanic environments," Remote Sens. Environ. **44**, 205–216 (1993).
3. L. L. Richardson, "Remote sensing of algal bloom dynamics," BioScience **46**, 492–501 (1996).
4. S. Thiemann and H. Kaufmann, "Lake water quality monitoring using hyperspectral airborne data—a semiempirical multisensor and multitemporal approach for the Mecklenburg Lake District, Germany," Remote Sens. Environ. **81**, 228–237 (2002).
5. M. K. Hamilton, C. O. Davis, W. J. Rhea, S. H. Pilorz, and K. L. Carder, "Estimating chlorophyll content and bathymetry of Lake Tahoe using AVIRIS data," Remote Sens. Environ. **44**, 217–230 (1993).
6. E. J. Hochberg and M. J. Atkinson, "Capabilities of remote sensors to classify coral, algae, and sand as pure and mixed spectra," Remote Sens. Environ. **85**, 174–189 (2003).
7. E. J. Hochberg and M. J. Atkinson, "Spectral discrimination of coral reef benthic communities," Coral reefs : Journal of the International Society for Reef Studies **19**, 164–171 (2000).
8. P. J. Mumby, W. Skirving, A. E. Strong, J. T. Hardy, E. F. LeDrew, E. J. Hochberg, R. P. Stumpf, and L. D. David, "Remote sensing of coral reefs and their physical environment," Mar. Pollution Bull. **48**, 219–228 (2004).
9. D. Lubin, W. Li, P. Dustan, C. H. Mazel, and K. Stamnes, "Spectral signatures of coral reefs: features from space," Remote Sens. Environ. **75**, 127–137 (2001).
10. S. Bagheri, M. Stein, and R. Dios, "Utility of hyperspectral data for bathymetric mapping in a turbid estuary," Int. J. Remote Sens. **19**, 1179–1188 (1998).
11. J. C. Sandidge and R. J. Holyer, "Coastal bathymetry from hyperspectral observations of water radiance," Remote Sens. Environ. **65**, 341–352 (1998).
12. D. Durand, J. Bijaoui, and F. Cauneau, "Optical remote sensing of shallow-water environmental parameters: a feasibility study," Remote Sens. Environ. **73**, 152–161 (2000).
13. E. M. Louchard, R. P. Reid, F. C. Stephens, C. O. Davis, R. A. Leathers, and T. V. Downes, "Optical remote sensing of benthic habitats and bathymetry in coastal environments at Lee Stocking Island, Bahamas: a comparative spectral classification approach," Limnol. Oceanogr. **48**, 511–521 (2003).

14. H. M. Dierssen, R. C. Zimmerman, R. A. Leathers, T. V. Downes, and C. O. Davis, "Ocean color remote sensing of seagrass and bathymetry in the Bahamas Banks by high-resolution airborne imagery," Limnol. Oceanogr. **48**, 444–455 (2003).
15. J. D. Hedley and P. J. Mumby, "A remote sensing method for resolving depth and subpixel composition of aquatic benthos," Limnol. Oceanogr. **48**, 480–488 (2003).
16. M. P. Lesser and C. D. Mobley, "Bathymetry, water optical properties, and benthic classification of coral reefs using hyperspectral imagery," Coral reefs : Journal of the International Society for Reef Studies **26**, 819–829 (2007).
17. J. Goodman and S. L. Ustin, "Classification of benthic composition in a coral reef environment using spectral unmixing," J. Appl. Remote Sens. **1**, 011501 (2007).
18. Z. Lee, K. Carder, C. D. Mobley, R. Steward, and J. Patch, "Hyperspectral remote sensing for shallow waters. 1. a semianalytical model," Appl. Opt. **37**, 6329–6338 (1998).
19. Z. Lee, K. Carder, C. D. Mobley, R. Steward, and J. Patch, "Hyperspectral remote sensing for shallow waters: 2. deriving bottom depths and water properties by optimization," Appl. Opt. **38**, 3831–3843 (1999).
20. C. D. Mobley, L. K. Sundman, C. O. Davis, J. H. Bowles, T. V. Downes, R. A. Leathers, M. J. Montes, W. P. Bisset, D. D. R. Kohler, R. P. Reid, E. M. Louchard, and A. Gleason, "Interpretation of hyperspectral remote-sensing imagery by spectrum matching and look-up tables," Appl. Opt. **44**, 3576–3592 (2005).
21. Z. Lee, K. L. Carder, R. F. Chen, and T. G. Peacock, "Properties of the water column and bottom derived from Airborne Visible Infrared Imaging Spectrometer (AVIRIS) data," J. Geophys. Res. **106**, 11639–11651 (2001).
22. Z. Lee and K. L. Carder, "Effect of spectral band numbers on the retrieval of water column and bottom properties from ocean color data," Appl. Opt. **41**, 2191–2201 (2002).
23. Z. Lee, B. Casey, R. Arnone, A. Weidemann, R. Parsons, M. J. Montes, B.-C. Gao, W. Goode, C. O. Davis, and J. Dye, "Water and bottom properties of a coastal environment derived from Hyperion data measured from the EO-1 spacecraft platform," J. Appl. Remote Sens. **1**, 011502 (2007).
24. J. A. Goodman, M. Velez-Reyes, S. Hunt, and R. Armstrong, "Development of a field test environment for the validation of coastal remote sensing algorithms: Enrique Reef, Puerto Rico," in *Remote Sensing of the Ocean, Sea Ice, and Large Water Regions*, C. R. Bostater, X. Neyt, S. P. Mertikas, and M. Velez-Reyes, eds. (SPIE, 2006), p. 8.
25. E. J. Hochberg, S. Andrefouet, and M. R. Tyler, "Sea surface correction of high spatial resolution Ikonos images to improve bottom mapping in near-shore environments," IEEE Trans. Geosci. Remote **41**, 1724–1729 (2003).
26. G. Vane, R. O. Green, T. G. Chrien, H. T. Enmark, E. G. Hansen, and W. M. Porter, "The airborne visible/infrared imaging spectrometer (AVIRIS)," Remote Sens. Environ. **44**, 127–143 (1993).
27. R. O. Green, M. L. Eastwood, C. M. Sarture, T. G. Chrien, M. Aronsson, B. J. Chippendale, J. A. Faust, B. E. Pavri, C. J. Chovit, M. Solis, M. R. Olah, and O. Williams, "Imaging spectroscopy and the Airborne Visible/Infrared Imaging Spectrometer (AVIRIS)," Remote Sens. Environ. **65**, 227–248 (1998).
28. J. L. Irish and W. J. Lillycrop, "Scanning laser mapping of the coastal zone: the SHOALS system," ISPRS J. Photogramm. Remote Sens. **54**, 123–129 (1999).
29. J. L. Irish, J. K. McClung, and W. J. Lillycrop, "Airborne lidar bathymetry: the SHOALS system," PIANC Bull. **103-2000**, 43–53 (2000).
30. J. A. Goodman and S. L. Ustin, "Underwater spectroscopy: methods and applications in a coral reef environment," presented at the 7th International Conference on Remote Sensing for Marine and Coastal Environments, Miami, Florida, USA, 20–22 May 2002.
31. J. A. Goodman and S. L. Ustin, "Acquisition of underwater reflectance measurements as ground truth," presented at the 11th JPL Airborne Earth Science Workshop, Jet Propulsion Laboratory, California, USA, 4–8 March 2002.
32. M. J. Montes, Naval Research Laboratory, Code 7232, Washington, D.C., 20375, (personal communication, 2005).
33. T. Heege and J. Fischer, "Sun glitter correction in remote sensing imaging spectrometry," in *SPIE Ocean Optics XV* (SPIE, 2000), p. 11.
34. L. Analytical Imaging and Geophysics, "ACORN 4.0 User's Guide," (ImSpec, LLC, Boulder, CO, 2002).
35. B.-C. Gao, M. J. Montes, Z. Ahmad, and C. O. Davis, "Atmospheric correction algorithm for hyperspectral remote sensing of ocean color from space," Appl. Opt. **39**, 887–896 (2000).
36. M. J. Montes, B.-C. Gao, and C. O. Davis, "A new algorithm for atmospheric correction of hyperspectral remote sensing data," Proc. SPIE **4383**, 23–30 (2001).
37. M. Montes, B.-C. Gao, and C. O. Davis, "Tafkaa atmospheric correction of hyperspectral data," Proc. SPIE **5159**, 188–197 (2003).
38. B.-C. Gao and A. F. H. Goetz, "Column atmospheric water vapor and vegetation liquid water retrievals from airborne imaging spectrometer data," J. Geophys. Res. **95**, 3549–3564 (1990).
39. B.-C. Gao, K. B. Heidebrecht, and A. F. H. Goetz, *Atmospheric Removal Program (ATREM) User's Guide* (University of Colorado at Boulder, 1992).
40. J. D. Hedley, A. R. Harborne, and P. J. Mumby, "Simple and robust removal of sun glint for mapping shallow-water benthos," Int. J. Remote Sens. **26**, 2107–2112 (2005).
41. K. J. Voss, C. D. Mobley, L. K. Sundman, J. E. Ivey, and C. H. Mazel, "The spectral upwelling radiance distribution in optically shallow waters," Limnol. Oceanogr. **48**, 364–373 (2003).